Chalcogenide Letters Vol. 12, No. 10, October 2015, p. 519 - 528

P-TYPE NANOSTRUCTURE PbS THIN FILMS PREPARED BY THE SILAR METHOD

F. GODE[a*], O. BAGLAYAN[b], E. GUNERI[c]
[a]*Mehmet Akif Ersoy University, Department of Physics, 15030 Burdur, Turkey*
[b]*Anadolu University, Department of Physics, 26470 Eskişehir, Turkey*
[c]*Erciyes University, Department of Primary Education, 38039 Kayseri, Turkey*

In this paper, we report on the structural, optical and electrical properties of nanocrystalline lead sulfide (PbS) thin films as a p-type semiconductor deposited on glass substrates at three different pH of the cationic precursor pH (pH = 10.22, 10.60 and 11.02) by the successive ionic layer adsorption and reaction (SILAR) method. The structure and morphology of the films are characterized by means of X-ray diffractions (XRD) patterns, micro-Raman spectroscopy, field-emission scanning electron microcopy (FE-SEM) and energy dispersive X-ray spectrometry (EDXS). The band gap and electrical properties are investigated by ultraviolet visible (UV-vis) diffuse reflectance spectroscopy and impedance spectroscopy. XRD patterns and micro-Raman spectra indicate that the deposited films have a cubic structure. EDXS data are used for analyses of chemical compositional of thin films. Micro-Raman spectra show the presence of eight vibrational active Raman modes for PbS thin films. FE-SEM images show a reduction in average grain size with the increment of pH values leads to the band gap width of the film increased from 1.73 eV to 2.37 eV whereas, the particle size decreases approximately from 133 nm to 13 nm a result of quantum confinement effect. Furthermore, room-temperature Hall measurements reveal an increase in electrical resistivity from 1.1×10^{3} Ω cm to 4.8×10^{6} Ω cm and a decrease in electrical conductivity 8.8×10^{-4} $(\Omega\ cm)^{-1}$ to 2.1×10^{-7} $(\Omega\ cm)^{-1}$ as well as carrier mobility from 720.1 $cm^2\ V^{-1}\ s^{-1}$ to 2.1 $cm^2\ V^{-1}\ s^{-1}$ and carrier concentration from 1.9×10^{15} cm^{-3} to 4.2×10^{12} cm^{-3} with increasing cationic precursor pH. Hall effect measurements and hot-probe experiments show that all films have p-type conductivity.

(Received September 8, 2015; Accepted October 21, 2015)

Keywords: PbS; SILAR; Raman spectroscopy; Optical properties; Electrical properties

1. Introduction

Metal chalcogenide thin films are fundamental part of micro/nanosized technologies and their fabrication and characterization with different types of majority charge carriers (n-type or p-type) have attracted the attention of researchers for many years. Thin film forms of these materials are used in solid state device fabrication. It is very difficult to observe how ‘p’ or ‘n’ type occured in these materials. Various mechanism are offered to explain the observed behaviour [1], but majority carrier type of metal chalcogenide thin films is still not clear and demand an in-depth study.

PbS thin film is an important binary IV–VI semiconductor with a narrow band gap (0.41 eV) and relatively large excitation Bohr radius (180 nm) [2], which results in strong quantum confinement of electrons and holes presents into the crystal lattice of PbS. It has band gap of the PbS thin films can be controlled simply by modifying particle size and shape. Quantum confinement in PbS thin films possessing significantly broader band gaps gives rise to many interesting structural, optical and electrical properties much different than their bulk counterparts,

*Corresponding author: ftmgode@gmail.com

making such films good candidates for light absorbers in solar cells, transistors, infrared detectors and biosensors [3–6], etc.

Various techniques on growing PbS thin films, such as sonication-assisted successive ionic layer adsorption and reaction (S-SILAR) [7], chemical bath deposition (CBD) [8], electro-deposition [9] and spray pyrolysis (SP) [10] have been developed. SILAR method for the deposition of PbS thin films from an aqueous solution like CBD method is a promising technique because of its simplicity, affordability, convenience for large area deposition and having easily-controllable parameters. In this method, the preparative conditions such as concentration, pH, temperature, immersion time and the number of immersion cycles, etc. are optimized to obtain good-quality PbS films [11].

A number of research attempts have been devoted to the production and characterization of PbS thin films. In our previous work [12], thermoluminescence properties of PbS thin films deposited by CBD method were reported. Patil et al [13] fabricated liquefied petroleum gas (LPG) using n-type PbS thin films with the band gap of 2.1 eV. Touati et al [14] investigated narrow optical band gap (0.72–1.46 eV) of p-type undoped and Zn doped PbS thin films. However, Obaid et al [15] prepared p-type PbS thin films with wide band gap ($1.6 \leq Eg \leq 2.7$ eV) using microwave-assisted CBD method. Morales-Fernández et al [16] studied electrical behavior of p-type PbS-based metal-oxide-semiconductor thin film transistors.

In this paper, p-type nanocrystalline PbS thin films at three different cationic precursor pH are produced on glass substrates by using SILAR method. This technique may be an alternative of vacuum based deposition techniques. Since SILAR enables one to build functional structures at atmospheric conditions using very simple and cost effective production tools. Therefore, we have been focused on the thin film deposition via SILAR. In the best of our knowledge, there are many reports for the production and characterization of p-type PbS thin films using this method, but there is no enough report on the Raman spectroscopy and electrical properties of these films.

2. Experimental details

The SILAR technique is based on the adsorption and reaction of ions from a solution and rinsing between each immersion cycles with deionised water to avoid homogeneous precipitation in the solution. The SILAR growth cycle involves four different steps such as adsorption, rinsing, reaction and rinsing again. Rinsing follows each reaction, which enables a heterogeneous reaction between the solid phase and the solvated ions in the solution.

The deposition of PbS thin films on glass substrates at room temperature (30 °C) is performed using 50 ml of 0.02 M lead(II) acetate trihydrate [$(CH_3COO)_2Pb + 3H_2O$], (Merck; 99.5%–102.0% purity) as a cationic precursor and 50 ml of 0.06 M thioacetamide [C_3CSNH_2], (Merck; ACS. Reagent purity) as an anionic precursor. The pH of the cationic precursor was adjusted to 10.22, 10.60 and 11.02 by adding ammonia solution [NH_3], (Merck; 25% purity) to it. The immersion time for both cationic and anionic precursor is 20 s, whereas the rinsing time between adsorption and reaction steps is 40 s. SILAR cycles and pH of the anionic precursor are held constant to be 25 times and approximately 9.54, respectively, in order to explore the effect of only the cationic precursor pH. The films grow more rapidly when the pH value is increased. For the deposition process, a well-cleaned glass substrate is immersed in the cationic precursor solution where Pb^{2+} ions are adsorbed on the substrate. After that, the substrate was rinsed with ion-exchanged water to remove unadsorbed Pb^{2+} ions from the substrate. Further, the substrate is immersed into the anionic precursor where S^{2-} ions diffuse from the solution in the difusion layer towards the solid-solution interface and react with Pb^{2+} to form PbS. After this, rinsing again in ion-exchange water to remove loose materials from the substrate follows. After this stage, the first SILAR growth cycle is completed. Repeating this procedure for the specified number of times, a thin film with the desired thickness can be deposited. Following deposition, the obtained films are dried in the oven at 60 °C for 1 hour and to be further characterized.

X-ray diffraction patterns of PbS films are obtained by using X-ray diffractometer (XRD) model Rigaku RadB in the scanning angle (2θ) range of 20-70 degrees with Cu$K\alpha$ radiation with a wavelength of λ = 1.54 Å. The Raman spectra are obtained by using two different Ne-ion laser

lines (532 and 633 nm) at room temperature using a Bruker Senterra spectrometer. Microstructural studies are performed by means of a field-emission scanning electron microscope (FE-SEM) (Ultra Plus Zeiss). Film composition is analyzed using an energy dispersive X-ray spectrometry (EDXS) analysis. Transmission spectra are recorded using a Perkin Elmer Lambda 4S spectrometer, providing a wavelength range from 400 to 1100 nm. The electrical properties of the PbS films are investigated at room temperature using a Hall effect measurement set up with a Van der Pauw geometry and a magnetic field of 0.54 T. The thicknesses of the films are measured by using a FE-SEM taking cross-sectional morphology of the PbS thin films.

3. Results and discussion

Fig. 1 shows the XRD patterns of the PbS thin films deposited at three different pH values of the cationic precursor (10.22, 10.60 and 11.02). The XRD patterns match well with that of the standard cubic (PDF No. 05-0592) structure. The observed diffraction peaks of cubic PbS are found at 2θ values of angles 25.88°, 29.97°, 43.03° and 50.95° corresponding to the lattice planes (111), (200), (220) and (311), respectively (Table 1). As can be seen, the intensity of the peak (200) is higher than the peak (111) in all films and the intensity of the peak (111) increases from 0.62 to 0.92 with increasing pH of the cationic precursor. Moreover, the intensity of the peaks which belong to the (220) and (311) planes increase with increasing pH.

The lattice constant (a) for the diffraction planes are obtained from the X-ray analysis using the following relationship for cubic crystals [17]:

$$a = d\sqrt{h^2 + k^2 + l^2} \tag{1}$$

where h, k and l are Miller indices. a is approximately found to be 5.95 Å (the reference data for bulk PbS is a = 5.94 Å) for all diffraction peaks.

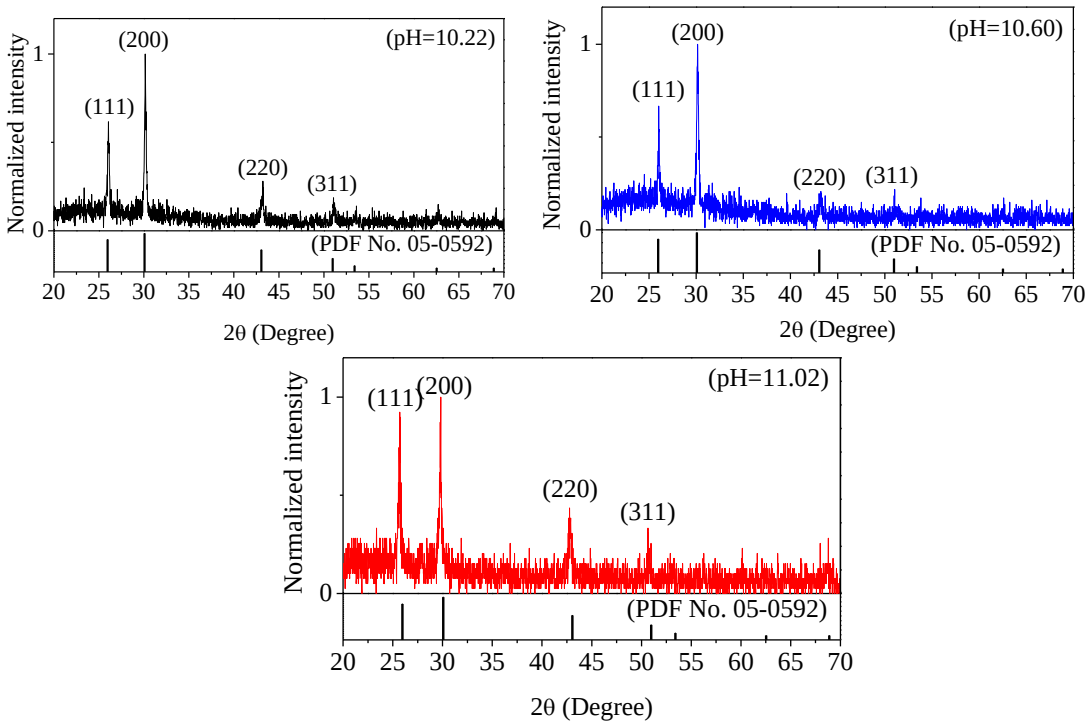

Fig. 1. X-ray diffraction pattern of PbS thin films deposited at three different pH values of the cationic precursor

Table 1. The diffraction angle (2θ), interplanar spacing (d), full with half maxima (FWHM), lattice parameter (a) and Miller indices (h k l) for PbS thin films

pH of cationic bath	2θ (°)	d (Å)	FWHM (°)	a (Å)	Peak
10.22	26.04	3.41	0.23	5.92	(1 1 1)
	30.14	2.96	0.22	5.92	(2 0 0)
	43.18	2.09	0.35	5.91	(2 2 0)
	51.10	1.79	0.38	5.94	(3 1 1)
10.60	26.04	3.42	0.19	5.92	(1 1 1)
	30.14	2.96	0.23	5.92	(2 0 0)
	43.10	2.10	0.52	5.94	(2 2 0)
	51.07	1.79	0.45	5.94	(3 1 1)
11.02	25.71	3.46	0.26	5.99	(1 1 1)
	29.79	2.99	0.20	5.98	(2 0 0)
	42.82	2.11	0.19	5.97	(2 2 0)
	50.68	1.80	0.24	5.97	(3 1 1)

Various structural parameters for PbS thin films deposited at different pH values of the cationic precursor calculated using standard formula are systematically presented in Table 1. The structural data are also in agreement with the reported data by Tohidi et al [18].

A definite existence of PbS in the produced films is demonstrated using Raman spectroscopy. Fig. 2 shows the room temperature Micro-Raman spectra of PbS thin films in the range of 80–1500 cm^{-1} measured using two different laser lines of 532 nm and 633 nm, respectively. Fig. 2 clearly shows that the scattering efficiency in former figüre is higher than that in latter one. Thus, the resonant nature of the scattering occurs in Fig 2(a) when a 532 nm laser line is used. However, Smith et al [19] reported an opposite behavior where the peak intensity of Raman phonons is almost two orders of magnitude higher for the 632.8 nm laser wavelength than for a 514.5 nm excitation. The discrepancy could be attributed to the polycrystalline nature of the PbS thin films in the present study, while Smith et al investigated a bulk PbS crystal (E_g = 0.41 eV at 300 K).

Furthermore, in Fig. 2, Micro-Raman spectra of deposited films indicates the presence of eight vibrational active Raman modes centered at around 94, 129, 187, 460, 826, 964, 970 and 1102 cm^{-1}, listed in Table 2. Raman peak at approximately 94 cm^{-1} might be attributed to a combination of longitudinal and transverse acoustic (LA + TA) phonon modes in PbS thin films. This mode also reported by Ovsyannikov et al [20], in which Raman phonon for $(PbS)_{1.18}(TiS_2)_2$ semiconductor structure is observed between 95 cm^{-1} and 96 cm^{-1}. The strong band located at 129 cm^{-1} might be originated from a combination of tansverse acoustic and optical (TA + TO) phonon modes. This band is also comparable with the results of Ovsyannikov et al (151 cm^{-1}) and Smith et al (154 cm^{-1}). The peak is observed at 187 cm^{-1} due to the combination of longitudinal and transverse (LO–TO) optical modes [21]. The peak, a shoulder at 460 cm^{-1} could be attributed to the longitudinal optical phonon mode (2LO) [22]. The less intensity first peak at 826 cm^{-1} is probably gypsum ($CaSO_4.2H_2O$) phase formed in producing PbS thin films. This phase is confirmed by He et al [23] at around 811 cm^{-1}. The less intensity second peak centered at 964 cm^{-1} may be related to $PbO.PbSO_4$ [24]. The less intensity third peak at 970 cm^{-1} is due to the anglesite $PbSO_4$ phase [24–27]. The last intensity peak centered at 1102 cm^{-1} may be assigned to $3PbO.PbSO_4.H_2O$ structure. Lara et al [26] detected this Raman phonon at 1096 cm^{-1}.

The physical properties of PbS nanoparticles are very sensitive to the variation of the grain size. Hence, the nanosized particles in the PbS films can produce significant modifications in the physical properties of the films. The reaction with atmospher O_2 and water (H_2O) leads to the formation of gypsum ($CaSO_4.2H_2O$) and oxysulfates complexes ($PbO.PbSO_4$, (anglesit) $PbSO_4$ and $3PbO.PbSO_4.H_2O$). However, XRD analysis shows no evidence of these species. This means that present phases may be amorphous.

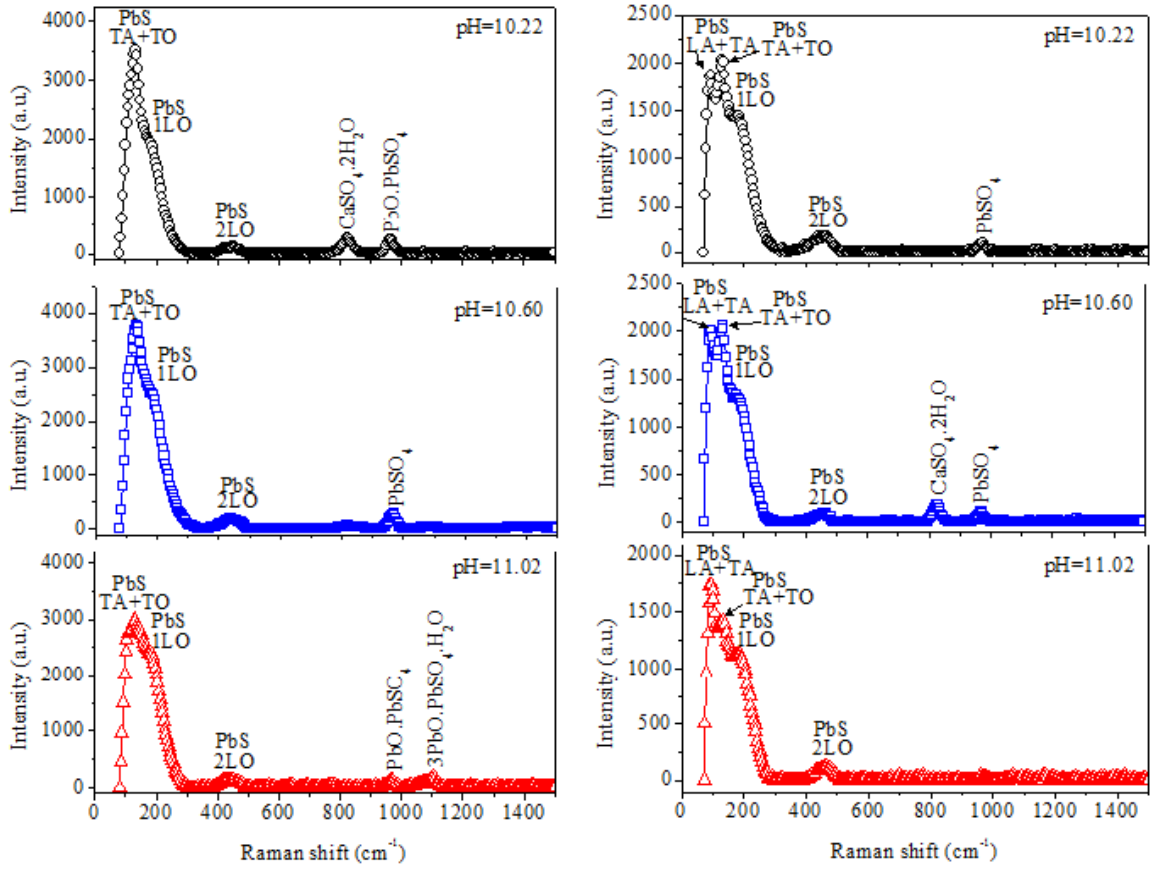

Fig. 2: Raman spectra of PbS thin films measured using two different laser lines as a function of the cationic precursor pH: (a) 532 nm, (b) 633 nm

Table 2. Observed Raman phonons of PbS thin films measured using two different laser lines

pH	532 nm laser line (cm^{-1})	633 nm laser line (cm^{-1})	Phonon origin	Phase
10.22	Not observed	98.3	LA(X) + TA(X)	PbS
	132.8	130.5	TA(X) + TO(X)	PbS
	188.0	183.4	LO–TO	PbS
	448.2	455.4	2LO	PbS
	825.0	Not observed	–	$CaSO_4.2H_2O$
	961.8	Not observed	–	$PbO.PbSO_4$
	Not observed	971.3	–	$PbSO_4$
10.60	Not observed	91.1	LA(X) + TA(X)	PbS
	130.5	128.2	TA(X) + TO(X)	PbS
	189.9	187.2	LO−TO	PbS
	444.0	466.7	2LO	PbS
	Not observed	828.0	–	$CaSO_4.2H_2O$
	968.6	968.6	–	$PbSO_4$
11.02	Not observed	93.8	LA(X) + TA(X)	PbS
	125.6	132.8	TA(X) + TO(X)	PbS
	Not observed	185.7	LO−TO	PbS
	441.4	464.4	2LO	PbS
	964.1	964.0	–	$PbO.PbSO_4$
	1102.0	Not observed	–	$3PbO.PbSO_4.H_2O$

Fig. 3 presents the surface morphology of the PbS thin films deposited at different pH values of the cationic precursor with the magnification of 100.000×. As can be clearly seen in these micrographs, the film surfaces consist of uniform granular structures with spherical-like shapes of different sizes and without vacancies. The film at pH = 11.02 shows some grapheme-like debris on the film surface due to the increasing pH compared with the others. Morphological investigations as a function of the cationic precursor pH clearly indicate that deposited films on the substrates are of nano-sizes and their diameters decrease approximately from 40−133 nm to 13−67 nm as shown in Table 3.

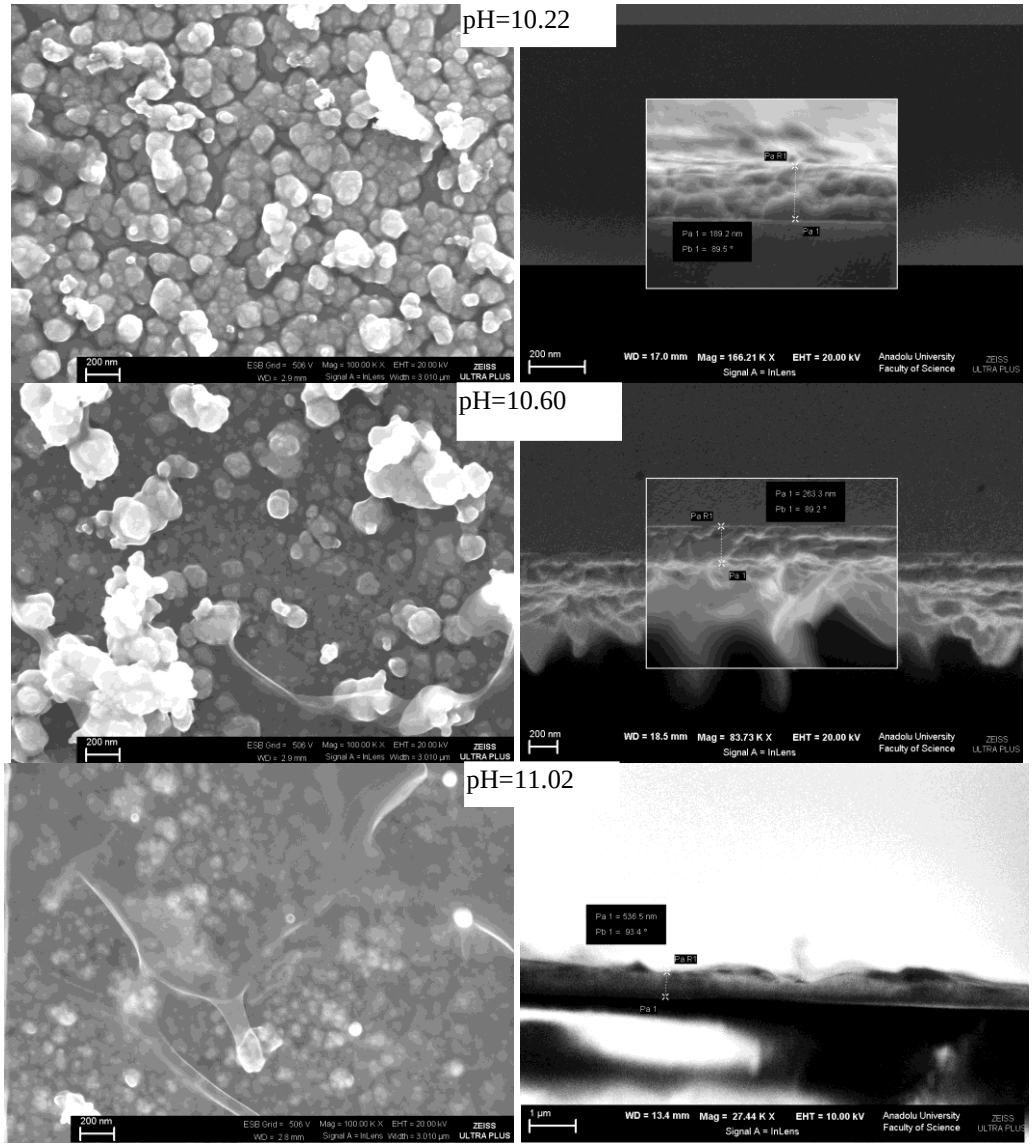

Fig. 3: (a) FE-SEM micrographs showing the surface morphology and (b) cross-sectional morphology of nanocrystalline PbS thin films deposited at different cationic precursor pH values

Quantitative analyses of the films are carried out using the EDXS technique to study stoichiometry of the films. The elemental analysis is carried out only for Pb and S in Table 3. Compositional analysis shows that S/Pb ratio increases from 0.69 to 0.97 as a function of cationic precursor pH. Compositional analysis of the film shows nearly stoichiometric film formation (S/Pb = 0.97) at pH = 11.02. It is observed that both decrease in grain size and increase in pH of the cationic precursor affect microstructure and composition of the films.

Table 3. Composition and grain size analysis of nanocrystalline PbS thin films deposited at different pH

pH	S/Pb	Atomic (%)		FE-SEM; *Grain size* (nm)
		S	Pb	
10.22	0.69	0.87	1.27	~40−133
10.60	0.78	4.32	5.54	~27−107
11.02	0.97	5.84	6.02	~13−67

The optical transmittance (*T*%) and absorption (*A*) spectra measured using UV-Vis spectrometer for the nanocrystalline PbS thin films deposited at room temperature are shown in Fig. 4(a) and (b), respectively. Moreover, Fig. 4(c) shows calculated reflectance spectra for the deposited films using *T* and *A* values. It is seen from Fig. 4 that all films exhibit very low transmission and very high absorption in the visible region. This property makes these films a good candidate as an absorber layer in solar cells. Moreover, the absorption edge shifts toward higher wavelengths as a result of the decrease in the band gap width due to the increasing pH of the cationic precursor.

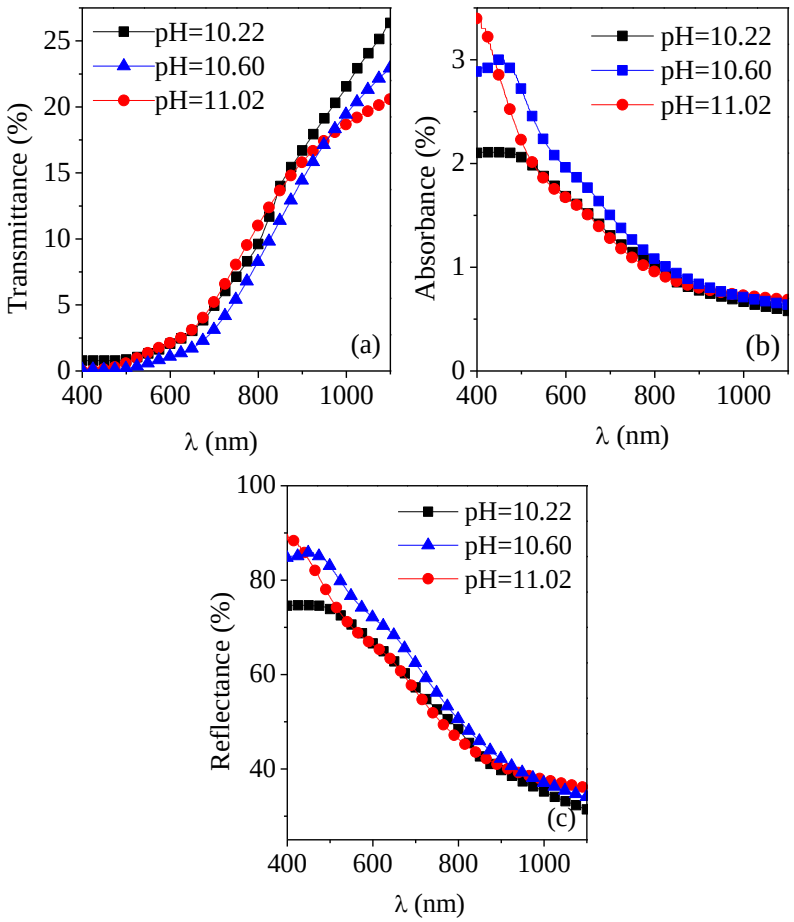

Fig. 4: The variation of (a) transmittance, (b) absorbance and (c) reflectance spectra of nanocrystalline PbS thin films obtained at different pH values of the cationic precursor with wavelength

The absorption coefficient (α) is given by the relation:

$$T = (1-R)\exp(-\alpha t) \qquad (2)$$

where *t* is the film thickness. The films having thicknesses of 189, 263 and 537 nm are obtained by changing the pH and detected from the cross-sectional FE-SEM analysis in Fig. 3(b). As can be seen from Fig. 5, film thickness depends so strongly on the pH. The absorption coefficient data are used to evaluate energy gap (E_g) using the relation [28]:

$$(\alpha h\nu)^2 = A(h\nu - E_g) \quad (3)$$

where, A is a proportionality constant and E_g is the direct transition band gap. From the $(\alpha h\nu)^2$ vs ($h\nu$) plot, the optical band gap energy is determined by extrapolating the linear portion of the graph, as shown in Fig. 5.

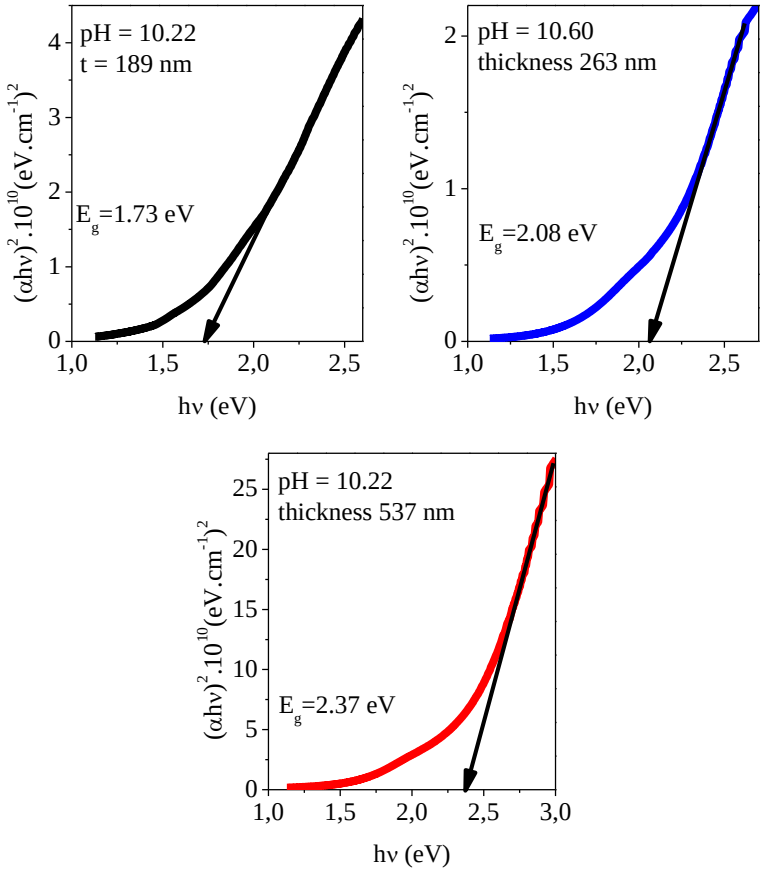

Fig. 5: Plot of $(\alpha h\nu)^2$ versus $(h\nu)$ for nanocrystalline PbS thin films deposited at various pH of the cationic precursor

The band gap width of the film increased from 1.73 eV to 2.37 eV with increasing pH of the cationic precursor. Considering our results, we have observed a reduction in average size of the grain with the increase in pH value seen in FE-SEM images. This size reduction can be attributed to the quantum confinement of PbS nanocrystals [29,30] this effect always tends to rise the optical gap values and decrease the number of intermediate levels between the valence and conduction bands in materials.

The electrical constants were obtained from Hall measurements, such as electrical resistivity (ρ) and conductivity (σ), as well as carrier mobility (μ) and concentration (N) of nanocrystalline PbS thin films with different cationic precursor pH, Table 4. From experimental data, it can be seen that the electrical resistivity increased from 1.1×10^{3} (Ω cm) to 4.8×10^{6} (Ω cm), whereas the electrical conductivity, mobility and carrier concentration decreased from 8.8×10^{-4} (Ω cm)$^{-1}$ to 2.1×10^{-7} (Ω cm)$^{-1}$ to from 720.1 cm^2 V^{-1} s^{-1} to 2.1 cm^2 V^{-1} s^{-1} and from 1.9×10^{15} cm^{-3} to 4.2×10^{12} cm^{-3}, respectively with increasing pH. The increase in resistivity may indicate an

improvement in film stoichiometry [31], seen in Table 3, or a decrease in electron density or mobility. Moreover, the reduction in conductivity can be explained by a decrease in grain size. This can be seen clearly in the FE-SEM micrographs in Fig. 3. The resistivity value at pH = 11.02 are consistent with reported data [10,12,32] involving PbS films grown by different techniques. In the present study, the observation of high electron mobility at pH = 10. 22 is related to a small number of lattice defects and a better ordered crystalline structure. Rogacheva et al [33] obtained higher carrier concentration (10^{16}–10^{18} cm^{-3}), but lower carrier mobility (425 cm^2 V^{-1} s^{-1}) than the present work. The decrease in grain size leads to an increase in grain boundary scattering, thus decreasing the mobility [34].

Table 4. Observed electrical resistivity, electrical conductivity, carrier mobility and the carrier concentration for the nanocrystalline PbS thin films.

pH	Resistivity (Ω cm)	Conductivity $(\Omega\ cm)^{-1}$	Hall mobility $(cm^2\ V^{-1}\ s^{-1})$	Carrier concentration (cm^{-3})
10.22	1.1×10^{3}	8.8×10^{-4}	720.1	1.9×10^{15}
10.60	3.8×10^{3}	2.6×10^{-4}	93.5	1.5×10^{14}
11.02	4.8×10^{6}	2.1×10^{-7}	2.1	4.2×10^{12}

In Raman spectra, PbS phase is clearly identified in the films as well as gypsum ($CaSO_4.2H_2O$) and oxysulfates complexes [$PbO(PbSO_4)$, ($PbSO_4$) and $3PbO(PbSO_4.H_2O)$]. The presence of these phases causes lattice defects and dislocations on the film surfaces and this case leads to a reduction in the electrical conductivity, as well as Hall mobility and carrier concentration.

The hot-probe experiment [35] was performed to determine majorty carrier type of the present films. This is a simple and efficient way to distinguish between n-type and p-type semiconductors using a heated probe and a standard multimeter. These experiments showed that all deposited nanocrystalline PbS thin films are p-type. Moreover, Hall effect measurements confirmed this p-type conductivity. The p-type conduction is generally attributed to the arising surface defects that are easily formed in the PbS phase (free holes from acceptors levels of lead vacancies). Similar behaviour is observed in $Cu_{2-x}S$ phase [36].

4. Conclusion

In summary, nanocrystalline PbS thin films were deposited by the SILAR method on glass substrates at room temperature with different cationic precursor pH. XRD patterns indicated that the all the films are monophasic free of deleterious phase and exhibited a cubic structure. The FE-SEM studies indicate that average PbS nanoparticle size with the pH of the cationic precursor decrease from 133 nm to 13 nm which results increasing band gap width from 1.73 eV to 2.37 eV. Raman spectra show PbS phase as well as gypsum ($CaSO_4.2H_2O$) and oxysulfates complexes [$PbO(PbSO_4)$, ($PbSO_4$) and $3PbO(PbSO_4.H_2O)$]. The results indicated that the grain size has an important impact on the structural, optical and electrical properties of PbS nanocrystalline. The Hall effect measurements and Hot-probe experiments show that all films have p-type conductivity. P-type nanocrystalline PbS thin films can be used for technological applications, such as absorber layers in solar cells because of suitable band gap (E_g < 3 eV), low transmittance in the visible range and low electrical resistivity.

Acknowledgement

This work was partially supported by the Mehmet Akif Ersoy University Scientific Research Projects Coordination Unit under the project number 0201-NAP-13. Authors would like to thank the Mehmet Akif Ersoy University for providing financial support to undertake this work.

References

[1] S. Pati, P. Banerji, S.B. Majumder, Int. J. Hydrogen Energy **39**, 15134 (2014).
[2] T. Torimoto, S. Takabayashi, H. Mori, S. Kuwabata, J. Electroanal. Chem. **522**, 33 (2002).
[3] B-M Kima, M-K Sona, S-K Kima, N-Y Honga, S. Parka, M-S Jeonga, H. Seob, K. Prabakara, H-J Kim, Electrochim. Acta **117**, 92 (2014).
[4] A. Carrillo-Castillo, A. Salas-Villasenor, I. Mejia, S. Aguirre-Tostado, B.E. Gnade, M.A. Quevedo-López, Thin Solid Films **520**, 3107 (2012).
[5] A.G.U. Perera, P.V.V. Jayaweera, G. Ariyawansa, S.G. Matsik, K. Tennakone, M. Buchanan, H.C. Liu, X.H. Su, P. Bhattacharya, Microelectron. J. **40**, 507 (2009).
[6] J. Li, Y. Tang, J. Yang, Z. Yang, Y. Zhang, X. Hu, Sens. Actuat. B **190**, 549 (2014).
[7] J. Wu, C. Tang, H. Xu, W. Yan, J. Alloys Comp. **633**, 83 (2015).
[8] R. Gertman, A. Osherov, Y. Golan, I. Visoly-Fisher, Thin Solid Films **550**, 149 (2014).
[9] N.R. Mathewsa, C. Ángeles–Chávez, M.A. Cortés-Jácome, J.A. Toledo Antonio, Electrochim. Acta **99**, 76 (2013).
[10] B. Thangaraju, P. Kaliannan, Semicond. Sci. Technol. **15**, 849 (2000).
[11] M. Ali Yıldırım, B. Güzeldir, A. Ates, M. Sağlam, Microelectron. Eng. **88**, 3075 (2011).
[12] F. Göde, E. Güneri, F.M. Emen, V.E. Kafadar, S. Ünlü, J. Lum. **147**, 41 (2014).
[13] S.V. Patil, P.R. Deshmukh, C.D. Lokhande, Sens. Actuat. B **156**, 450 (2011).
[14] B. Touati, A. Gassoumi, S. Alfaify, N. Kamoun-Turki, Mat. Sci. Semicon. Proc. **34,** 82 (2015).
[15] A.S. Obaid, M.A. Mahdi, Y. Yusof, M. Bououdina, Z. Hassan, Mat. Sci. Semicon. Proc. **16**, 971 (2013).
[16] I.E. Morales-Fernández, M.I. Medina-Montes, L.A. González, B. Gnade, M.A. Quevedo-López, R. Ramírez-Bon, Thin Solid Films **519**, 512 (2010).
[17] B. Pejova, A. Tanuevski, I. Grozdanov, J. Solid State Chem. **177**, 4785 (2004).
[18] T. Tohidi, K. Jamshidi-Ghaleh, A. Namdar, R. Abdi-Ghaleh, Mat. Sci. Semicon. Proc. **25**, 197 (2014).
[19] G.D. Smith, S. Firth, R.J.H. Clark, M. Cardona, J. Appl. Phys. **92**, 4375 (2002).
[20] S.V. Ovsyannikov, V.V. Shchennikov, A. Cantarero, A. Cros, A.N. Titov, Mater. Sci. Eng. A **462**, 422 (2007).
[21] Y. Bencherif, A. Boukra, A. Zaoui, M. Ferhat, Infrared Phys. Technol. **54**, 39 (2011).
[22] R. Sherwin, R.J.H. Clark, R. Lauck, M. Cardona, Solid State Commun. **134**, 565 (2005).
[23] L. He, N. Wang, X. Zhao, T. Zhou, Y. Xia, J. Liang, B. Rong, J. Archaeol. Sci. **39**, 1809 (2012).
[24] E. Schreck, V. Dappe, G. Sarret, S. Sobanska, D. Nowak, J. Nowak, E.A. Stefaniak, V. Magnin, V. Ranieri, C. Dumat, Sci. Total Environ. **476–477**, 667 (2014).
[25] B. Han, A. Xie, Q. Yu, F. Huanga, Y. Shen, L. Zhu, Appl. Surf. Sci. **261**, 623 (2012).
[26] R.H. Lara, R. Briones, M.G. Monroy, M. Mullet, B. Humbert, M. Dossot, G.M. Naja, R. Cruz, Sci. Total Environ. **409**, 3971 (2011).
[27] A. Godelitsas, N. Stamatelos-Samios, M. Kokkoris, E. Chatzitheodorid, Nucl. Instr. Meth. Phys. Res. B **269**, 3074 (2011).
[28] R.H. Misho, W.A. Murad, Sol. Energy Mater. Sol. Cells **27**, 335 (1992).
[29] B-R Hyun, Y-W. Zhong, A.C. Bartnik, L. Sun, H.D. Abruña, F.W. Wise, J.D. Goodreau, J.R. Matthews, T.M. Leslie, N.F. Borrelli, ACS Nano, **2**(11), 2206 (2008).
[30] H. Chung, H. Choi, D. Kim, S. Jeong, J. Kim, J. Phys. Chem. C **119**, 7517 (2015).
[31] A.A. Ramadan, R.D. Gould, A. Ashour, Int. J. Electron. 73 (1992) 717.
[32] A. Mondal, N. Mukherjee, Mater. Lett. **60**, 2672 (2006).
[33] E.I. Rogacheva, O.N. Nashchekina, Y.O. Vekhov, M.S. Dresselhaus, S.B. Cronin, Thin Solid Films **423**, 115 (2003).
[34] H.S. Choi, S.H. Jeon, H.J. Kim, J.K. Shin, C.J. Kim, U.I. Chung, Appl. Phys. Lett. **100**, 173501 (2012).
[35] F. Göde Physica B **406**, 1653 (2011).
[36] G. Liu, T. Schulmeyer, J. Brotz, A. Klein, W. Jaegermann, Thin Solid Films **431/432,** 477 (2003).